Geophys. J. Int. (1994) **116,** 527–537

Inversion of 3-D DC resistivity data using an approximate inverse mapping

Yaoguo Li and Douglas W. Oldenburg

UBC—Geophysical Inversion Facility, Department of Geophysics and Astronomy, University of British Columbia, Vancouver, V6T IZ4. *Canada*

Accepted 1993 July 15. Received 1993 June 30; in original form 1992 November 12

SUMMARY

We present an iterative algorithm for inverting 3-D pole–pole DC resistivity data. The algorithm utilizes an AIM (approximate inverse mapping) formalism and iterative inversions are carried out by performing updates in both model space (AIM—MS) and data space (AIM—DS) by using an approximate inverse mapping with an exact forward mapping. In the approximate inverse mapping, the potential anomaly is expressed as a depth integral of the logarithmic conductivity perturbation convolved horizontally with a known kernel. Fourier transforming the data equation decouples wavenumber components and the Fourier transform of the conductivity anomaly is recovered by performing 1-D linear inversions at each wavenumber. Inverse Fourier transforming the 1-D inversion results produces the sought conductivity. The AIM methodology avoids the generation and inversion of a full 3-D sensitivity matrix and is consequently fast and efficient. Only one forward modelling is performed at each iteration. The algorithm is tested with synthetic data and a field data set from an epithermal region.

Key words: approximate inverse, Born approximation, conductivity, 3-D, DC resistivity, inversion, mineral exploration.

INTRODUCTION

The goal of this paper is to develop an efficient method for inverting direct current (DC) potential data that have been acquired in an areal survey at the surface of the earth. A typical experiment might be by an E-SCAN survey which is usually carried out over a pre-designed regular grid. Each grid point is occupied in turn by a current source and the surface potentials are measured at the remaining grid points. Thus an E-SCAN data set consists of many groups of potential measurements from a common source and the total number of potentials observed is generally about 10 000.

The interpretation of a DC data set often requires that an acceptable conductivity model be constructed through an inversion algorithm. The inversion of DC data is a non-linear problem and the most common approach has been to first linearize the problem and then to construct the model iteratively using Newton's method. This requires that, at each iteration, the sensitivity matrix (or the Fréchet derivatives) be computed so that the change in the data can be mapped to a change in the model. Since there are typically 10 000 data and likely more conductivity cells to be solved for, the sensitivity matrix is large. A model perturbation is then found by solving a system of equations. These operations of computing and inverting a large matrix pose difficulties in practical applications and motivate the search for a simpler solution.

In a previous paper (Li & Oldenburg 1992) we presented an efficient method which maps a set of potential data to a conductivity model without resorting to the generation and inversion of a 3-D sensitivity matrix. That approximate inversion was formulated by first gathering the potential data associated with a specific current and potential pole–pole separation and orientation. The data maps were Fourier transformed and a succession of 1-D inversions were carried out in the wavenumber domain to produce the Fourier transform of the model. The desired 3-D conductivity was obtained by inverse Fourier transforming. Application of this approximate inversion to numerous synthetic and field models has shown that the conductivity output often displays some of the major features of the true conductivity but details are incorrect and generally the model does not adequately reproduce the data. The output qualifies as a conductivity image but is not generally an acceptable inversion result.

The goal of this paper is to keep the approximate inversion and its efficient computational attributes but to use it in an iterative algorithm so that an acceptable model is generated. The approximate inverse mapping (AIM)

inversion developed by Oldenburg & Ellis (1991) provides the framework for such an approach. In the AIM inversion, an approximate inverse mapping is used in conjunction with an exact forward mapping to update the model successively so that the final model will adequately reproduce the observed data. The algorithm iterates towards such an acceptable model without necessarily computing and inverting a large sensitivity matrix. There are two ways in which the AIM inversion can utilize the approximate inverse mapping, namely, AIM—MS and AIM—DS. In AIM—MS, a perturbation in model space is sought so that the updated model more closely predicts the observed data. In AIM—DS, a perturbation in data space is sought such that the application of the approximate inverse mapping to the updated data generates the desired model. The two essential components of the AIM inversion are an exact forward mapping and an approximate inverse mapping. For the DC inversion problem we shall use the finite difference modelling algorithm of Dey & Morrison (1979) as the exact forward mapping, and the approximate 3-D inversion as the approximate inverse mapping.

The paper begins with brief discussions about the AIM formalism, the approximate inverse mapping, and the forward modelling. We next outline the procedure of the AIM inversion for the 3-D DC resistivity data and then apply the inversion algorithm to a synthetic data set contaminated with noise and a field data set from an epithermal deposit area.

AIM FORMALISM

The basic philosophy and examples of the AIM approach are given in detail in Oldenburg & Ellis (1991). Here we summarize only the relevant equations needed for our work. Let $\mathcal{F}$ denote the forward mapping which maps an element m of model space to an element e in data space and let $\tilde{\mathcal{F}}^{-1}$ denote the approximate inverse mapping. Let e^{obs} be the observed data and let $m^{(n)}$ be the model and $e^{(n)}$ be the predicted data at the nth iteration,

$$\mathcal{F}[m^{(n)}] = e^{(n)} \tag{1}$$

Application of the approximate inverse mapping $\tilde{\mathcal{F}}^{-1}$ to e^{obs} and $e^{(n)}$ yields $\tilde{m}^{\text{obs}}$ and $\tilde{m}^{(n)}$, respectively. That is,

$$\tilde{\mathcal{F}}^{-1}(e^{\text{obs}}] = \tilde{m}^{\text{obs}}, \tag{2}$$

$$\tilde{\mathcal{F}}^{-1}[e^{(n)}] = \tilde{m}^{(n)} \tag{3}$$

The updated model $m^{(n+1)}$ derived through AIM—MS is given by

$$m^{(n+1)} = m^{(n)} + (\tilde{m}^{\text{obs}} - \tilde{m}^{(n)}). \tag{4}$$

The iteration starts with an initial model $m^{(0)}$, which can be supplied by $\tilde{m}^{\text{obs}}$.

In AIM—DS, if the modified data are $\tilde{e}^{(n)}$ at the nth iteration, the updated data are given by

$$\tilde{e}^{(n+1)} = e^{\text{obs}} + \tilde{e}^{(n)} - e^{(n)}. \tag{5}$$

The new model is obtained by applying $\tilde{\mathcal{F}}^{-1}$ to the updated data, that is,

$$m^{(n+1)} = \tilde{\mathcal{F}}^{-1}[\tilde{e}^{(n+1)}]. \tag{6}$$

The iteration starts with any reasonable initial data $\tilde{e}^{(0)}$, however, the choice $\tilde{e}^{(0)} = e^{\text{obs}}$ is appropriate.

Equations (4) and (5) define respectively the iterative process of the AIM—MS and AIM—DS inversions and are readily carried out once the forward mapping $\mathcal{F}$ and the approximate inverse mapping $\tilde{\mathcal{F}}^{-1}$ are defined.

FORWARD MAPPING

Our forward mapping is the finite difference forward modelling algorithm presented by Dey & Morrison (1979). The conductivity model represented by a finite rectangular region is discretized into prismatic cells by a 3-D orthogonal mesh. Each cell is assigned a constant conductivity value. The algorithm can work with general 3-D conductivity models but the current source must be placed on a nodal point. The resulting potential is calculated at all other nodal points. The current sink is assumed to be at infinity.

The mesh for forward modelling is primarily defined by the geometry of the E-SCAN survey. The measurement grid on the surface is used to define the horizontal grid of the mesh and a vertical partitioning is chosen to define layers of cells to a depth $z_{\max}$. The value of $z_{\max}$ is chosen so that the kernel functions for the inverse mapping all have negligible amplitude at that depth. We enlarge this core mesh into an extended mesh so that the boundary condition in the forward modelling algorithm can be handled. Usually three padding cells of increasing size towards the boundary are used.

INVERSE MAPPING

Our approximate inverse mapping is the approximate 3-D inversion developed by Li & Oldenburg (1992). We briefly outline the method here and also develop a slightly different form suitable for use in conjunction with a finite difference forward modelling algorithm. Readers are referred to the original paper and Li (1992) for more details on the algorithm.

Let the electrical conductivity in a lower half-space be $\sigma(\mathbf{r}) = \sigma_0\mu(\mathbf{r})$, where σ_0 is the conductivity of a uniform background and $\mu(\mathbf{r})$ is a dimensionless function of spatial position $\mathbf{r}$. Then under the Born approximation, the relative potential anomaly defined by the ratio of secondary to primary potential, $\delta\phi = \phi_s/\phi_p$, measured by a pole–pole array over a flat surface is given by

$$\delta\phi(\mathbf{r}_0, \mathbf{l}) = \int_0^\infty \ln \mu(\mathbf{r}) \otimes\otimes\, g(\mathbf{r}, \mathbf{l})\, dz, \tag{7}$$

where $\otimes\otimes$ denotes the 2-D convolution operation and $g(\mathbf{r}, \mathbf{l})$ is the kernel function

$$\begin{aligned} g(\mathbf{r}, \mathbf{l}) &= -\frac{1}{\pi}\nabla\frac{1}{|\mathbf{r}+\mathbf{l}|}\cdot\nabla\frac{1}{|\mathbf{r}-\mathbf{l}|} \\ &= -\frac{l[(x+l_x)(x-l_x)+(y+l_y)(y-l_y)+z^2]}{\pi[(x+l_x)^2+(y+l_y)^2+z^2]^{3/2}} \\ &\quad\times[(x-l_x)^2+(y-l_y)^2+z^2]^{-3/2} \end{aligned} \tag{8}$$

The datum is recorded at the midpoint of an array specified by the current and potential electrodes at $\mathbf{r}_s$ and $\mathbf{r}_{\text{obs}}$ respectively. $\mathbf{l}$ defines the relative position of the two electrodes such that $\mathbf{r}_s - \mathbf{r}_{\text{obs}} = 2\mathbf{l}$.

Taking the 2-D Fourier transform of eq. (7) and applying the convolution theorem yields

$$\tilde{e}_j(p, q) = \int_0^\infty \tilde{m}(p, q, z)\tilde{g}_j(p, q, z)\, dz, \qquad j = 1, \ldots, n_l \quad (9)$$

where (p, q) are the wavenumbers in the x and y directions and

$$\tilde{e}_j(p, q) = \mathcal{F}_{xy}[\delta\phi(\mathbf{r}_0, \mathbf{l}_j)], \qquad j = 1, \ldots, n_l,$$
$$\tilde{m}(p, q, z) = \mathcal{F}_{xy}[\ln \mu(\mathbf{r})],$$
$$\tilde{g}_j(p, q, z) = \mathcal{F}_{xy}[g(\mathbf{r}, \mathbf{l}_j)], \qquad j = 1, \ldots, n_l,$$

where $\mathcal{F}_{xy}[*]$ denotes the 2-D Fourier transform. The index j identifies the jth pole–pole array. We denote the number of distinct pole–pole arrays by n_l. If n_l pole–pole data maps are available, there are n_l (complex) data at each wavenumber (p, q) and a linear inversion can be used to recover $\tilde{m}(p, q, z)$. The 3-D conductivity model in the spatial domain is then obtained by applying an inverse 2-D Fourier transform to $\tilde{m}$ at all depths. This process therefore solves a 3-D inverse problem in the spatial domain by a sequence of 1-D inversions in the wavenumber domain.

To implement the inverse mapping, several steps are required. First, a background conductivity needs to be estimated so that the relative anomaly can be computed. The calculated anomaly maps are then interpolated to a common grid and Fourier transformed to yield the data in the wavenumber domain. Secondly, the kernel functions need to be evaluated. This is done numerically. For each pole–pole array specified by $\mathbf{l}_j$, we sample the spatial kernel $g(\mathbf{r}, \mathbf{l}_j)$ over a fine horizontal grid at a set of depths. The sampled function at each depth is then Fourier transformed to generate the wavenumber kernel function $\tilde{g}_j(p, q, z)$. Thirdly, once the data and the kernels are generated, 1-D inversions are performed to recover $\tilde{m}$.

To be consistent with the assumed Born approximation, we invert for a conductivity model which deviates as little as possible from the background. Such a model minimizes

$$\Phi(\mu) = \int_x\int_y\int_z w(z)[\ln \mu(\mathbf{r})]^2\, dx\, dy\, dz,$$

subject to the data constraints, where $w(z)$ is a user-specified weighting function. By Parseval's theorem, this is equivalent to minimizing the quantity

$$\Phi(\tilde{m}) = \int_0^\infty w(z)\, |\tilde{m}(p, q, z)|^2\, dz \quad (10)$$

subject to the data constraints (9) at each point (p, q), in the wavenumber domain. Therefore, at each wavenumber we choose to find the particular model $\tilde{m}(p, q, z)$ which minimizes

$$\Phi(\tilde{m}) = \int_0^\infty w(z)\, |\tilde{m}(p, q, z)|^2\, dz + \theta^{-1} \sum_{j=1}^{n_l} \left| \tilde{e}_j - \int_0^\infty \tilde{g}_j(p, q, z)\tilde{m}(p, q, z)\, dz \right|^2, \quad (11)$$

where θ is a ridge regression parameter. The weighting function $w(z)$ is generally of the form $1/(z + z_0)$ so that model variation in the vertical direction is essentially measured on a logarithmic scale. The quantity z_0 is added to avoid the singularity at the surface.

The forward mapping is a finite difference modelling algorithm using cells of constant conductivity. It is desirable therefore that the inversion output has the same form. Correspondingly we choose a depth partition for the inverse problem which coincides with the vertical mesh in the forward mapping, $(z_0, \ldots, z_n)$, where $z_0 = 0$ and $z_n = z_{\max}$. Boxcar functions

$$b_k(z) = \begin{cases} 1, & z \in [z_{k-1}, z_k], \\ 0, & \text{otherwise.} \end{cases} \qquad k = 1, \ldots, n \quad (12)$$

are defined as the basis functions for the model space and the model is expanded as

$$\tilde{m}(p, q, z) = \sum_{k=1}^{n} \tilde{m}_k b_k(z), \quad (13)$$

where the coefficients $\tilde{m}_k$ are now constants to be determined. The weighting function is also chosen to be consistent with the model expanded in $\{b_k(z)\}$:

$$w(z) = \sum_{k=1}^{n} w_k b_k(z),$$

where w_k are a set of positive real numbers.

Substituting into (11) yields the new objective function

$$\Phi(\tilde{m}) = \mathbf{m}^{\mathrm{H}}\mathbf{W}\mathbf{m} + \theta^{-1}(\mathbf{G}\mathbf{m} - \mathbf{e})^{\mathrm{H}}(\mathbf{G}\mathbf{m} - \mathbf{e}), \quad (14)$$

where $\mathbf{m} = (\tilde{m}_1, \ldots, \tilde{m}_n)$, and the jkth element of the real matrix $\mathbf{G}$ is given by the integral of the jth kernel over the kth depth interval,

$$\tilde{g}_j^k(p, q) = \int_{z_{k-1}}^{z_k} \tilde{g}_j(p, q, z)\, dz.$$

The weighting matrix $\mathbf{W} = \mathrm{diag}\,[w_1(z_1 - z_0), \ldots, w_n(z_n - z_{n-1})]$ and 'H' denotes the complex conjugate transpose. Minimizing (14) with respect to model parameters $\mathbf{m}$ using a variational principle yields

$$(\mathbf{G}^{\mathrm{T}}\mathbf{G} + \theta\mathbf{W})\mathbf{m} = \mathbf{G}^{\mathrm{T}}\mathbf{e}.$$

Since $\mathbf{W}$ is positive definite and diagonal, $\mathbf{W}^{-1/2}$ exists and is diagonal. Therefore, the above equation may be written as

$$(\mathbf{G}_w^{\mathrm{T}}\mathbf{G}_w + \theta\mathbf{I})\mathbf{m}_w = \mathbf{G}_w^{\mathrm{T}}\mathbf{e}, \quad (15)$$

where $\mathbf{G}_w = \mathbf{W}^{-1/2}\mathbf{G}$ and $\mathbf{m}_w = \mathbf{W}^{1/2}\mathbf{m}$.

Equation (15) is solved efficiently using the singular value decomposition (SVD) of the matrix $\mathbf{G}_w$. Let $\mathbf{G}_w = \mathbf{U}\mathbf{S}\mathbf{V}^{\mathrm{T}}$, where $\mathbf{S}$ is a diagonal matrix of singular values, $\mathbf{S} = \mathrm{diag}\,(s_1, \ldots, s_{n_r})$ and n_r is the effective rank of the matrix $\mathbf{G}_w$. $\mathbf{U}$ and $\mathbf{V}$ are left and right singular vector matrices, respectively. The solution of (15) is then given by

$$\mathbf{m}_w = \mathbf{V}\mathbf{S}(\mathbf{S}^2 + \theta\mathbf{I})^{-1}\mathbf{U}^{\mathrm{T}}\mathbf{e}, \quad (16)$$

and the final model is obtained by unweighting $\mathbf{m}_w$:

$$\mathbf{m} = \mathbf{W}^{-1/2}\mathbf{m}_w.$$

The model norm can be computed by

$$\|\tilde{m}\|^2 = \sum_{i=1}^{n_r} |\hat{e}_i|^2 \left(\frac{s_i}{s_i^2 + \theta}\right)^2, \quad (17)$$

where $\hat{e}_i$ are the elements of the rotated data vector $\hat{\mathbf{e}} = \mathbf{U}^{\mathrm{T}}\mathbf{e}$ and the ridge regression parameter θ is chosen so that it corresponds to the onset of the rapid model norm increase.

The conductivity in the spatial domain is obtained by inverse Fourier transforming the function $\tilde{m}(p, q, z)$. It attains a discrete point representation in the horizontal directions by the nature of the fast Fourier transform. Beneath each surface nodal point, the model is piecewise constant in accordance with the vertical meshing. The logarithmic conductivity $\ln(\sigma)$ is assumed to be represented by piecewise bilinear interpolations in the horizontal directions. A conductivity value is then derived from the integrated average of $\ln(\sigma)$ within each cell of the forward mesh. This value is assigned to the corresponding cell as the conductivity value recovered by the approximate inverse mapping.

IMPLEMENTATION

With the forward and inverse mapping being defined, the next step is to define the data and the model of the AIM inversion. Although $\tilde{\mathcal{F}}^{-1}$ takes the relative potential anomaly as data and produces a conductivity model to which the forward mapping $\mathcal{F}$ is applied, the data and the model for the AIM algorithm can be defined differently. For AIM—MS, we choose to work with the logarithm of the conductivity and the model is composed of the set of the logarithmic conductivity values $\ln(\sigma_{ijk})$ $(i = 1, \ldots, M_x, j = 1, \ldots, M_y, k = 1, \ldots, M_z)$, where M_x, M_y, M_z are respectively the number of cells in the x, y, and z direction. Working with logarithmic conductivities is advantageous in accommodating the variation of conductivity over a great range and also it ensures the positivity of the conductivity model. In addition, it is consistent with the logarithmic conductivity perturbation sought in approximate inverse mapping. Thus, the iterative eq. (4) takes the form

$$\ln[\sigma^{(n+1)}] = \ln(\tilde{\sigma}^{\text{obs}}) + \ln[\sigma^{(n)}] - \ln[\tilde{\sigma}^{(n)}]. \tag{18}$$

Given the total potential $\phi_j(x, y)$ associated with n_t pole–pole array configurations, the data for the AIM—DS inversion are defined as the logarithm of the potential values, $\ln[\phi_j(x, y)](j = 1, \ldots, n_t)$. Eq. (5) becomes

$$\ln[\bar{\phi}^{(n+1)}] = \ln[\bar{\phi}^{(n)}] + \ln(\phi^{\text{obs}}) - \ln[\phi^{(n)}]. \tag{19}$$

Adopting the logarithmic potential as the data eases the task of data interpolation and ensures that the updated potential is always positive.

The flow charts in Fig. 1 show the procedures for applying the AIM inversions to the 3-D E-SCAN DC resistivity data. The termination criteria are based upon data misfit, model norm or a maximum number of iterations.

SYNTHETIC EXAMPLE OF THE AIM INVERSION

To illustrate the inversion of the E-SCAN DC resistivity data using the AIM formalism, we first apply both AIM algorithms to a synthetic data set with added noise. The synthetic data are generated over a five-prism model. A simulated E-SCAN data set is computed over a 21×21 grid with a grid spacing $\Delta = 50\,m$. From this, eight pole–pole data maps are formed in both x and y directions with array separation equal to $n\Delta$ $(n = 1, \ldots, 8)$. Five maps are also formed in xy and yx diagonal directions with separations equal to $n\sqrt{2}\Delta$ $(n = 1, \ldots, 5)$. The 26 data maps contain a total of 8804 potential data. Next, uncorrelated Gaussian noise is added to each of the 26 data maps. The noise has zero mean and standard deviation equal to 5 per cent of the corresponding total potential. Fig. 2 shows one cross-section and two depth slices of the synthetic model. (The gray scales in this and all the following figures are in $\log_{10}(\sigma)$). The cross-section cuts through the four major prisms and the two

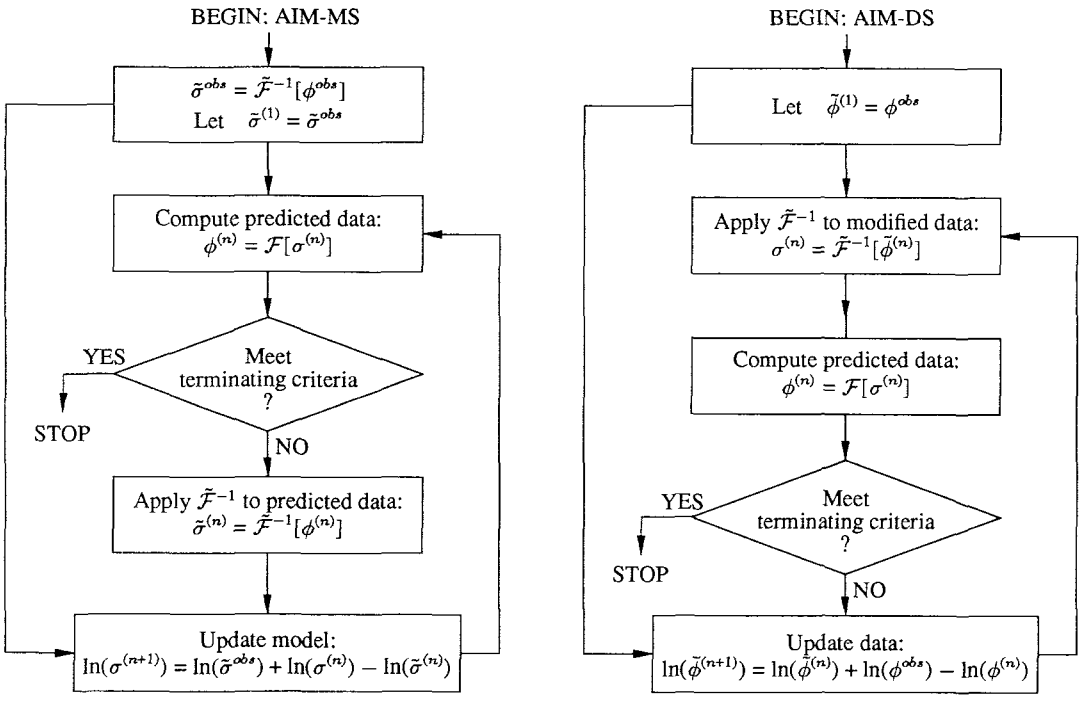

Figure 1. Flow charts for AIM—MS and AIM—DS algorithms.

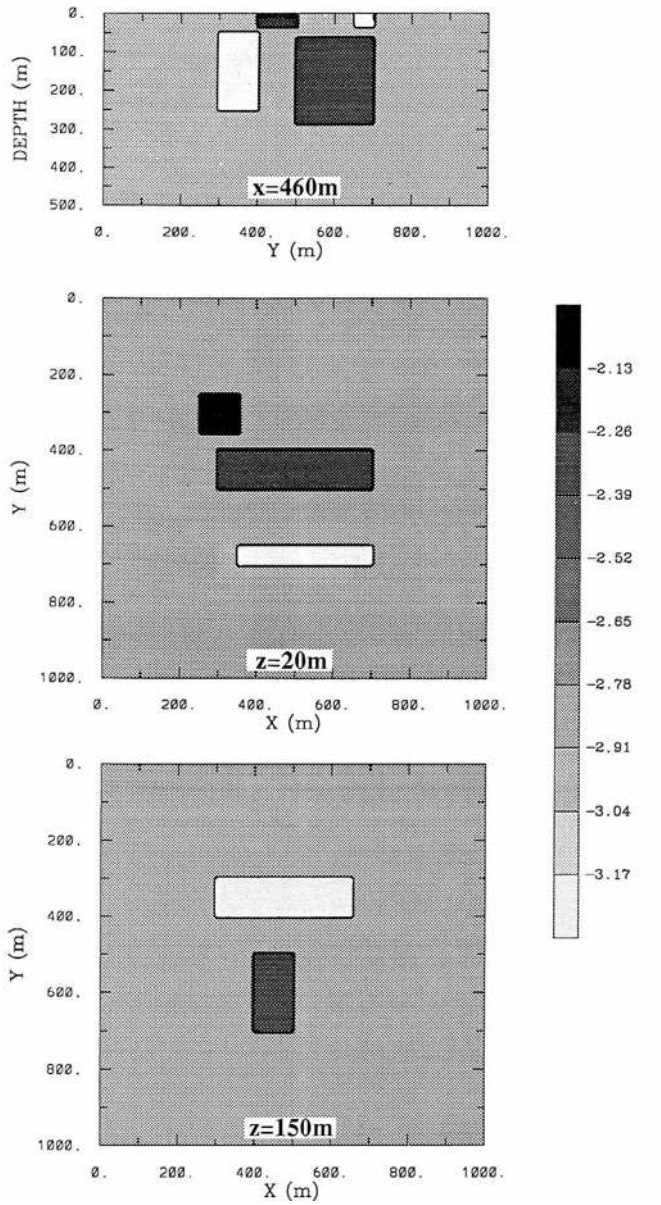

Figure 2. Three slices of the true conductivity model consisting of five prisms in a uniform half-space. The three surface prisms are placed to simulate the near-surface variations in the conductivity and the buried prisms are the targets. The top panel shows a cross-section which intersects with four major prisms and the middle and bottom panels are depth slices at 20 m and 150 m, respectively.

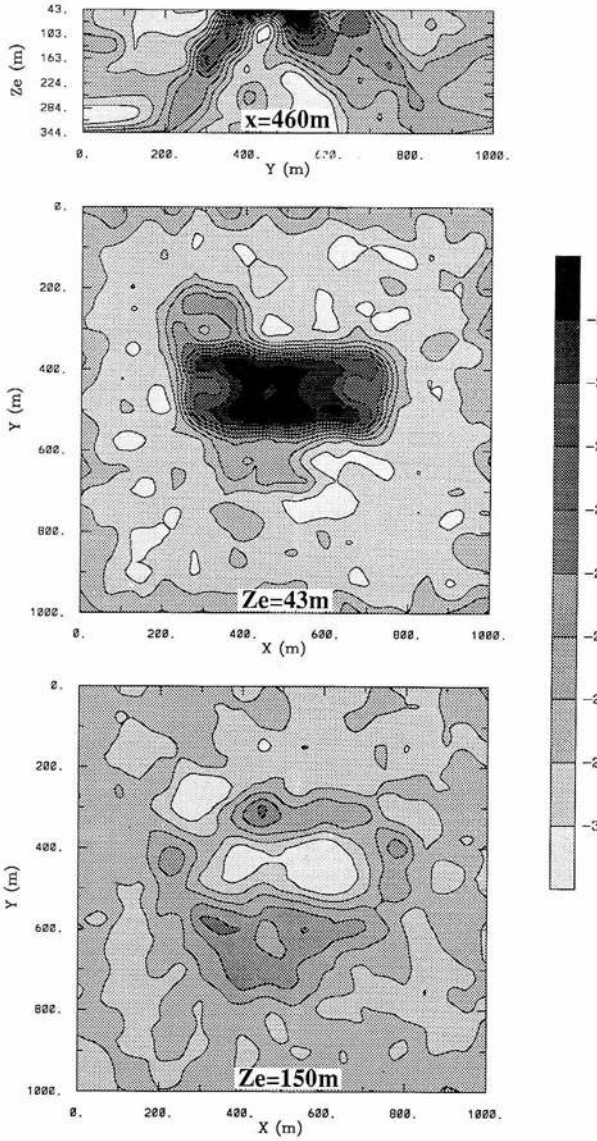

Figure 3. Apparent conductivity data from the five-prism model. The pseudo-section in the top panel is generated using the data from pole–pole arrays aligned in the y direction. The plan maps are generated by averaging the log apparent conductivity data from x and y directions. The pseudo-depth is taken as 0.86 times the electrode separation. 5 per cent Gaussian independent noise has been added to the data.

depth slices indicate the lateral locations of the prisms. Fig. 3 shows three slices of the apparent conductivity data. The data are plotted with a pseudo-depth equal to 0.86 times the array separation. The pseudo-section coincides with the first slice in Fig. 2 and is formed using apparent conductivity for current and potential electrodes oriented in the y direction. The two plan maps are formed by averaging the logarithmic apparent conductivities from electrodes oriented in the x and y directions.

The AIM—MS algorithm is first applied to the data set. For the forward-modelling mesh we use a horizontal grid that is the same as the data grid, a vertical grid of 21 nodes corresponding to cells whose thicknesses progressively increase in depth, and three padding cells appended to all sides and the bottom. The total number of cells in the inversion is 15 548. Throughout the inversion, the half-space conductivity has been held at the correct value of 1 mS m^{-1}. The weighting function used in the 1-D inversions is $w(z) = 1/(z + z_0)$, where $z_0 = 10$ m. The convergence curves for the inversion are shown in Fig. 4. A steady reduction of the misfit is observed in panel (a) and the expected χ^2 misfit (8804) is achieved after four iterations. Panels (b) and (c) show the norm of the model and the model perturbation for successive iterations. The resulting models from the first and the fourth iteration are shown in Figs 5 and 6 respectively. These are to be compared with the true conductivity model in Fig. 2 and the apparent conductivity data in Fig. 3. The

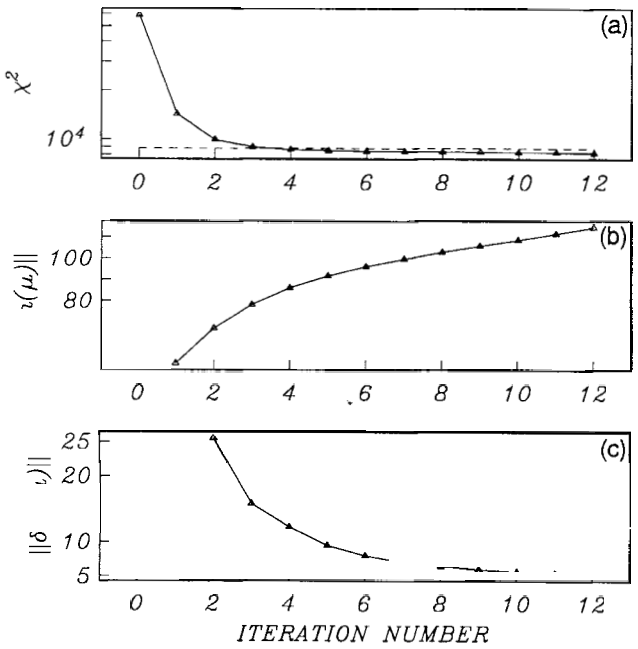

Figure 4. Convergence plots of the AIM—MS inversion applied to noisy data from the five-prism model. Panel (a) shows the χ^2 data misfit, the dashed line indicates the expected misfit. Panels (b) and (c) show the model norm and the norm of the model perturbation respectively as functions of iteration.

first iteration recovers an image of the conductivity model. The surface anomalies and the buried conductive anomaly are clearly defined but the buried resistive anomaly is barely visible. The amplitudes of the anomalies are substantially less than that of the true model. Further updates by the AIM algorithm greatly improve the result. The final model as shown in Fig. 6 recovers all the conductivity anomalies and has a dynamic range comparable with that in the true model. The added noise has introduced spurious structures in the model. Such distortion is especially strong near the surface. In terms of the model recovery, however, the inversion is quite successful.

The AIM—DS inversion is next applied to the data set with the same mesh and half-space conductivity. Again the expected χ^2 is achieved in four iterations. The convergence curve and the final model (from the fourth iteration) are shown in Figs 7 and 8, respectively. A steady reduction of the misfit is observed in the first few iterations and all anomalous blocks are well defined in the final model. The model is very similar to that from the AIM—MS inversion but it has less structure near the surface. This is consistent with the fact that the AIM—DS model is obtained through a single application of the inverse mapping whereas the AIM—MS model is built up by a series of perturbations.

Three primary observations can be made from these two inversions. In the AIM—MS inversion, the final model is built up by a sequence of model perturbations and, hence, no minimization of the model norm is performed. In the AIM—DS, the l_2 norm of the model is minimized but the horizontal variation is only controlled by limiting the largest wavenumber components. Without explicit control over the structural complexity of the conductivity model, the

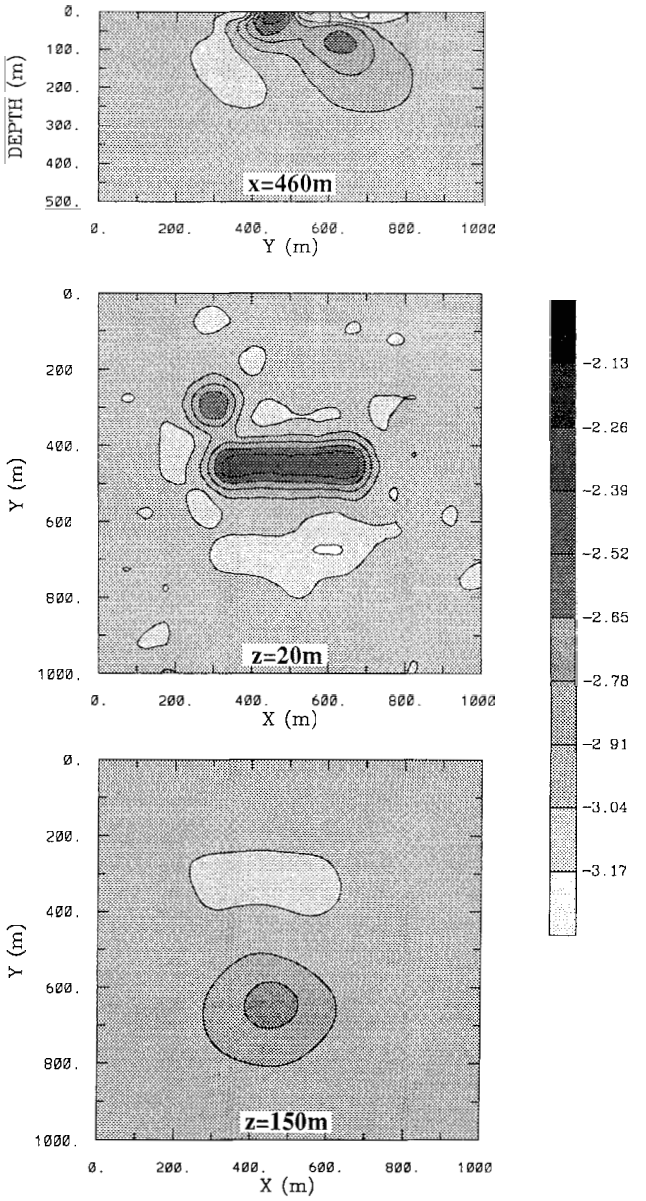

Figure 5. The conductivity model recovered from the first iteration. This is equivalent to the result obtained by applying the approximate inverse mapping to the observed data. The top panel is a cross-section at $x = 460$ m, which intersects four prisms and the middle and bottom panels are horizontal slices at 20 m and 150 m depths respectively.

spurious structures introduced by the noise are not totally suppressed through the regularization in the inversion. However, these structures appear to be uncorrelated and become progressively weaker as the depth increases. This is judged to be a direct result of the approximate inverse mapping and the inversion mesh employed in the inversion. The kernel functions in the wavenumber domain decay more rapidly with depth at higher wavenumbers. Meanwhile, the energy of the data is concentrated in the lower wavenumber band whereas the energy of the noise is spread throughout the entire band. Thus at the lower wavenumber, the signal-to-noise ratio is higher and the recovered model components have fewer spurious features. Structures at

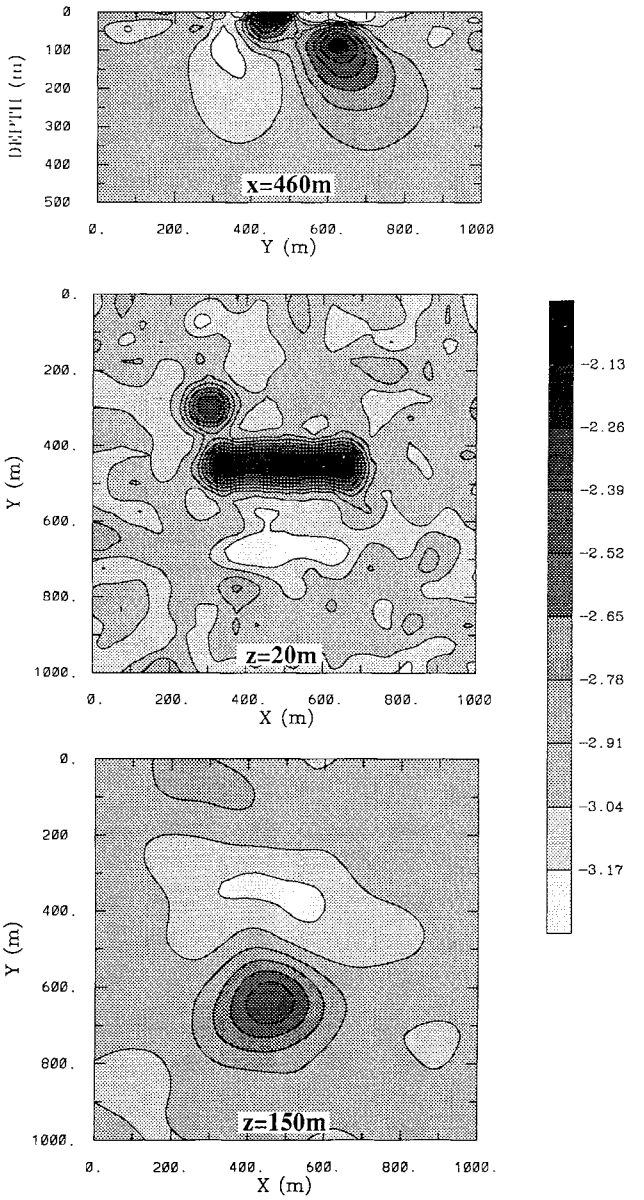

Figure 6. The conductivity model recovered from the fourth iteration of AIM—MS inversion. This is selected as the final model since the expected χ^2 misfit is achieved. Comparison with the results from iteration 1 in Fig. 5 shows the significant improvement achieved by the further updates with the AIM algorithm.

depth are dominated by these low-wavenumber components. On the other hand, signal-to-noise ratio decreases as the wavenumber increases. Since the kernel functions for higher wavenumbers are sensitive to shallower regions, this can produce structural complexity near the surface if it is allowed in the model. Such is the case with the current example since the inversion mesh has very fine vertical partitioning near the surface and the corresponding cells therefore permit small-scale variations. This suggests that these undesirable features can be suppressed by using relatively thick cells near the surface. They can also be partially treated by applying a lowpass filtering to the model with the cut-off wavenumber decreasing with the depth. The type of filter and the cut-off wavenumber will depend upon

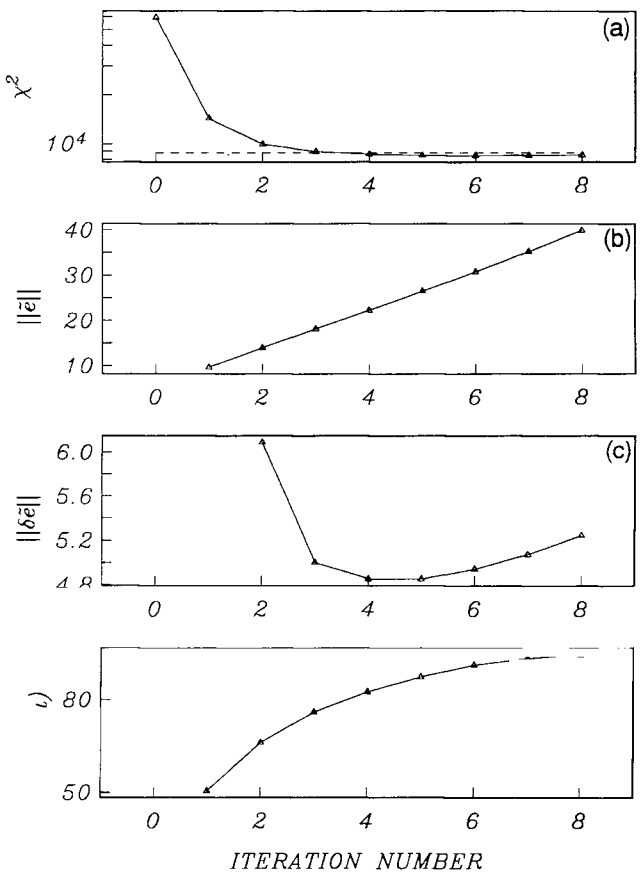

Figure 7. Convergence plots of the AIM—DS inversion applied to noisy data from the five-prism model. Panel (a) shows the misfit as a function of iteration. The dashed line indicates the expected χ^2 misfit. Panels (b) and (c) are the norm of the modified data and the norm of the data perturbation respectively. Panel (d) shows the model norm.

the spectrum of data and the noise and, hence, will be problem dependent and is not rigorously investigated here.

The results from the AIM—MS and AIM—DS inversion are very similar in the above two inversions. This may have resulted because in the implementation presented here the two algorithms share a common initial model produced by a single application of the approximate inverse mapping and, as seen in Figs 4 and 7, a major reduction of the data misfit is achieved in this first iteration. Further iterations tend to reduce the misfit slightly by introducing small-scale refinements and increasing the amplitude of the anomalous structures.

The inversion in both AIM—MS and AIM—DS was continued even after the expected misfit was achieved. This allowed us to explore some aspects of the convergence of the AIM algorithm. Although the data misfit in AIM—MS inversion is still decreasing by the 12th iteration, the data misfit begins to increase slightly in AIM—DS inversion from the sixth iteration (see Fig. 7). This increase coincides with the increase in the norm of the data perturbation and indicates the alorithm has begun to diverge. This behaviour is to be anticipated. It has been shown (Bertero, De Mol & Pike 1988) that the degree of regularization is inversely proportional to the number of iterations for an iterative inversion without explicit regularization. Such is the case

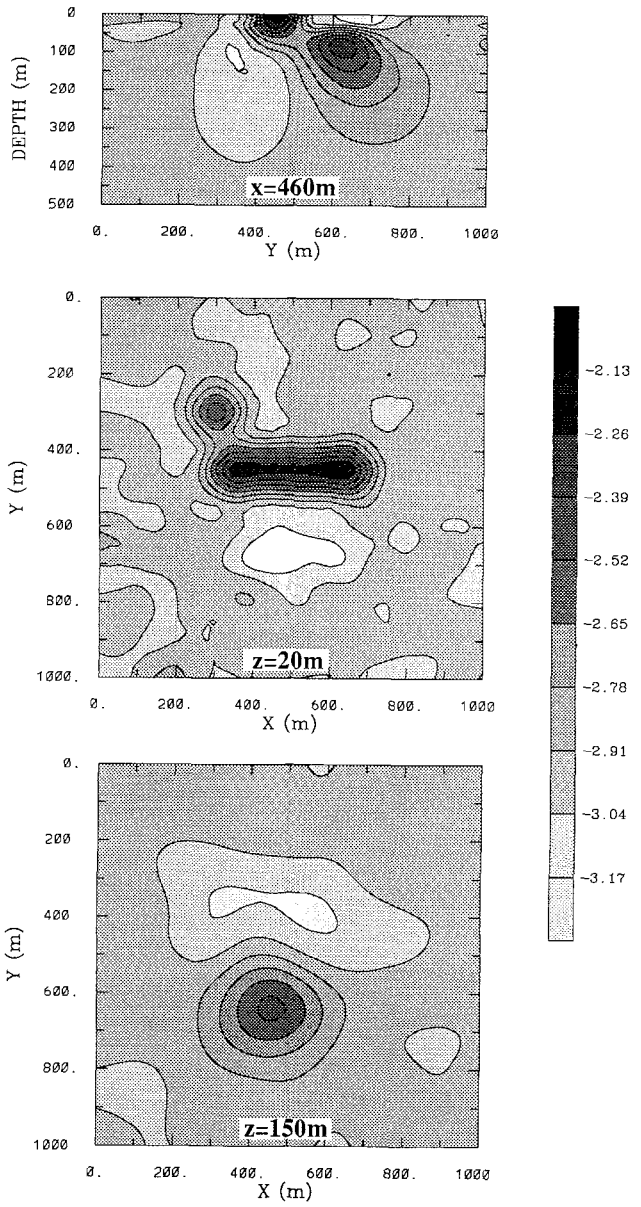

Figure 8. The conductivity model recovered from the fourth iteration of AIM—DS inversion applied to the data from the five-prism model. The cross-section is at $x = 460$ m and the two horizontal slices are at 20 m and 150 m depths respectively. In contrast to the results from AIM—MS inversion shown in Fig. 6, this model has less noisy structure near the surface.

with the AIM inversion as applied here. Since this specific implementation of the AIM inversion does not explicitly minimize the model norm subject to a prescribed data misfit, the prolonged iterations increase the structural complexity of the model but do not necessarily improve the data misfit. This suggests that the inversion should be terminated once the expected misfit is achieved or, if the expected misfit cannot be reached, the onset of the increase in misfit should serve as the criterion for termination.

FIELD-DATA EXAMPLE

As a second example, we apply the AIM inversion to a set of field data acquired in an epithermal area associated with mineral deposits. Such hydrothermal deposits most commonly occur within the upper 600 m in areas with well-developed fracture and fault systems. Existing faults or fractures act as feeders of hot fluid which alter the host rock and deposits minerals. Ore is formed in the alteration zones, which often expand in the upper portion to form cone-like or mushroom-shaped features with deep 'roots'. Precious metal deposits are frequently associated with silicification brought about by hydrothermal alteration.

Because of the highly resistive nature of the veins and silicified zones, the ore deposits exhibit localized conductivity anomalies as typical signatures in the DC resistivity experiment. The area in which the survey was completed was covered with eluvium and there are few indications about the existence of the silicified zones. The E-SCAN survey was employed to map the silicification zones and possibly fault structures. The data were acquired over a 32×35 grid with 91.4 m spacing. The 'infinite' electrodes, current sink and potential reference, were about 7 km from the centre of the grid. This is too near for the resultant data to be regarded as pole–pole and therefore the data were first corrected for biases in the potential introduced by these electrodes. A correction was made by subtracting the contribution of the 'infinite' electrodes over a uniform half-space having an estimated conductivity of 40 mS m^{-1}.

The processed data are gathered into 26 maps corresponding to electrode pairs in the x- and y-grid directions and in the 45° diagonal directions. The pole–pole separations ranged from 1 to 10 basic grid spacings, which are sufficiently large for the depth of interest. As the last processing step prior to inversion we smooth each data map using a 2-D spline interpolation. Since the data error is uncertain, the generalized cross-validation (GCV) technique (Craven & Wahba 1979) is used to estimate the optimum degree of smoothing to be applied. These smoothed data maps, containing 6825 potentials are used in the inversion as the observed data. Fig. 9 shows one plan map and two pseudo-sections of apparent conductivities calculated from the processed data. The plan section is formed using data in the x direction and corresponds to a pseudo-depth of 150 m. We point out that much of the dominating structure on the west in this plan section is caused by near-surface features and persists from the shortest offset data. The data, therefore, offers few indications to the actual structure at this depth. The positions of the pseudo-section are marked in the plan map and coincide with two drill sections which provide some geological information.

The AIM—DS algorithm is applied to the processed data maps to construct a 3-D conductivity model. The forward mesh has a uniform vertical partitioning with a spacing of 30 m down to 600 m. With a three-cell extension zone, this results in a mesh of $38 \times 41 \times 24$ nodal points. Thus the inversion has a total of 34 040 unknowns. An AIM—DS inversion is carried out for six iterations. For the 1-D inversions we used a weighting function $w(z) = 1/(z + z_0)$, where $z_0 = 20$ m. The best-fitting half-space conductivity of 52.6 mS m^{-1} from the 26 data maps is used as the background-conductivity value.

In order to stabilize the iterative process, we have also introduced a relaxation parameter to control the step-size of the data update. The quantity $[e^{\text{obs}} - e^{(n)}]$ in eq. (5) can be considered to provide both the direction and the step-size

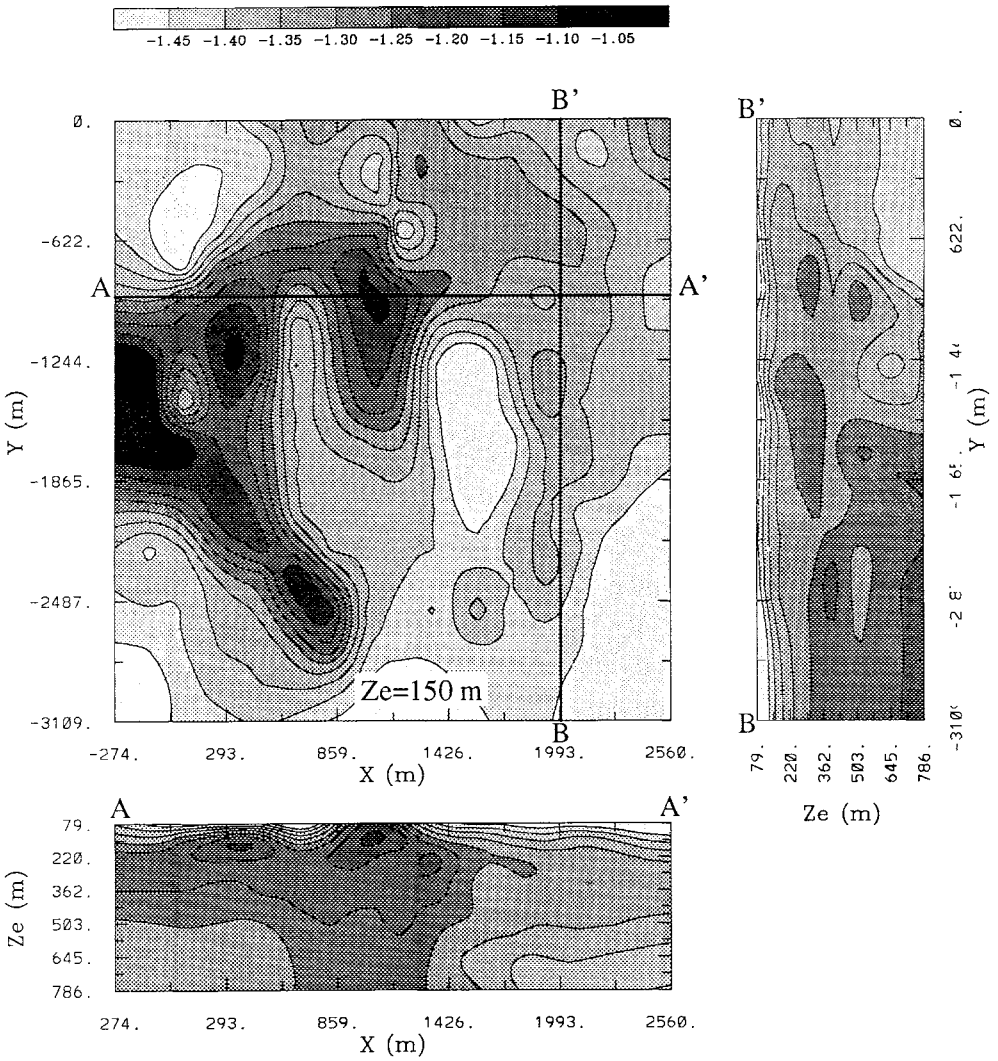

Figure 9. One plan and two pseudo-sections of apparent conductivity data. The plan section is generated from data aligned in the x direction and corresponds to a pseudo-depth of 150 m. The two pseudo-sections are taken at the location marked in the plan section and are plotted in their respective orientations.

for the perturbation. We can perturb the data in this direction but control the stepsize. That is, the data can be updated by, $\tilde{e}^{(n+1)} = \tilde{e}^{(n)} + \omega[e^{\text{obs}} - e^{(n)}]$, where ω is the relaxation parameter. A choice of ω less than unity should prevent an over correction of the data and keep the iterative process stable. A relaxation with $\omega = 0.6$ is chosen. The inversion steadily reduced the data misfit form the initial half-space value of 36 to 12 per cent. Fig. 10 shows the misfit, model norm, and data perturbation measured in their respective norms as the inversion progresses. It is noticed that the major reduction of the misfit is achieved in the first two iterations. After four iterations, there is little change in the misfit, but the model norm does increase considerably. This is similar to the synthetic example, where both the data misfit and the norm of the data perturbation exhibit a slight increase at the later iterations. For these reasons, we take the model from the fourth iteration as the final model.

Fig. 11 shows a plan section and two cross-sections from this model. The cross-sections coincide in position with those of the pseudo-sections in Fig. 9. The recovered conductivity model has many structural details at shallow depth but becomes increasingly smooth at greater depth. The benefits of carrying out the inversion can be seen by comparing Figs 9 and 11. The model obtained from the inversion displays many structures not visible or clear in the apparent conductivity sections, and clear definition of various conductive and resistive units. Ideally, these definitions should be related to different lithologic units using the information obtained from drilling. Although five major lithologic units have been identified in this region, their geo-electric properties are still uncertain. This, together with the limited availability of drilling information, makes verification difficult at this stage. Nevertheless there are some qualitative comparisons that can be made.

The resistive layer immediately below the surface as shown in the sections in Fig. 11 covers almost the entire model with varying degree of continuity. This layer, which is likely the eluvium, is uniform on the eastern part but becomes variable toward the west as it is interspaced with small-scale conductive features. Beneath this resistive layer

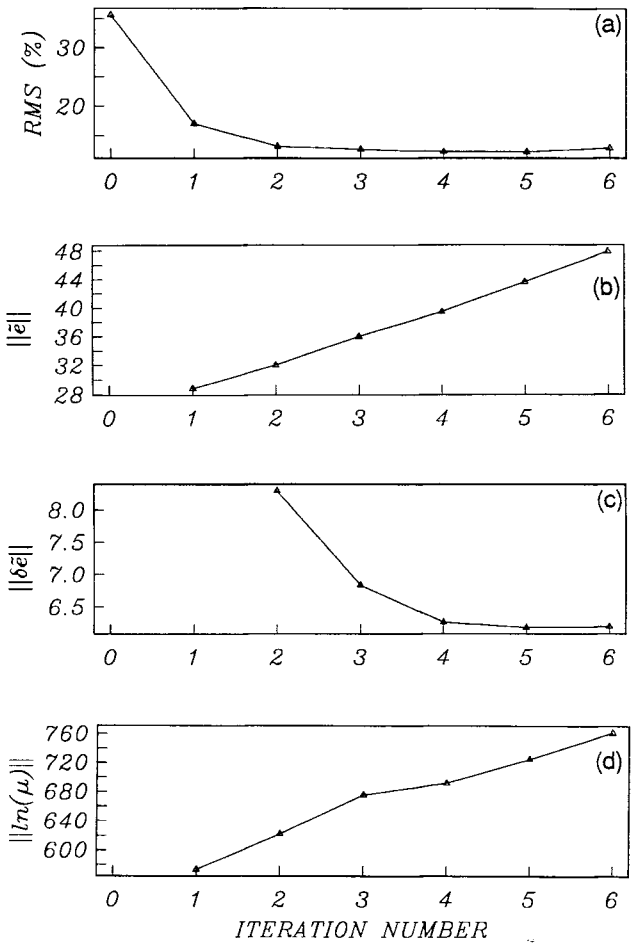

Figure 10. Convergence plots of the AIM—DS inversion of the field data. Panel (a) is the RMS data misfit. Panels (b) and (c) are respectively the norms of the modified data and the data perturbation. Panel (d) is the norm of the model. Note that both data misfit and data perturbation start to increase after four iterations.

there are various localized conductive and resistive units. Borehole information in the section AA′ indicates that there is a fault between $x = 1000$ m and $x = 1200$ m. The steep contour lines seen in the cross-section near that location, and the large horizontal change of conductivity, may reflect the existence of the fault. In the section BB′, the sharp conductivity contrast near $y = -400$ m may indicate the position of a fault known from borehole information. It is possible that the three conductive features on a semi-circle in the north-west portion on the planview map in Fig. 11 are connected with the two faults and the general hydrothermal system.

We conclude that the algorithm has performed satisfactorily. The inversion starts from a best-fitting half-space model with a misfit of 36 per cent, and constructs a sequence of minimum norm models which steadily reduce the misfit to 12 per cent. Such a fit is not overly poor for a field data set. Owing to the nature of the algorithm, there is little chance that large-scale spurious structures are introduced and therefore, features appearing in the model are most likely required by the observed data and may reflect true large-scale conductivity variations.

DISCUSSION

The formalism of the AIM inversion is successfully applied to the 3-D DC resistivity inverse problem and both AIM—MS and AIM—DS iterative inversion algorithms have been constructed to invert E-SCAN data for a 3-D conductivity model. On a synthetic test the algorithms have succeeded in producing conductivity models which adequately reproduce the data within the tolerance of the associated errors, and represent the true models with reasonable fidelity. In the inversion of a field data set, 6825 potential data are used to construct a conductivity model having 34 040 cells. The achieved model produces an RMS relative misfit of 12 per cent and exhibits various structures and geo-electrical units that are not visible in the apparent conductivity images. A few known structures are reflected in the model.

In general, the AIM—DS is advantageous in comparison with AIM—MS inversion. AIM—MS generates the final model by a series of model perturbations and there is no explicit control over the norm of the model. As a result, the model from an AIM—MS inversion can acquire excessive structure. The AIM—DS inversion, however, generates the final model from a single application of the approximate inverse mapping and can, therefore, produce a smoother model if a norm of the model is explicitly minimized in the inverse mapping.

Our inversion algorithms have combined the advantages of the approximate 3-D inversion and the AIM formalism. The kernel functions for the approximate 3-D inversion are computed at the first iteration and stored for subsequent iterations. As a result, the inverse mapping at each iteration is rapid, since its solution in the wavenumber domain takes only a small fraction of the time needed for computing kernel functions. In addition, the AIM formalism requires only one forward mapping at each iteration and this greatly reduces the computational effort. For the field data set where 6825 potential data were used to recover 34 040 parameters, each iteration took less than 300 min CPU time on a 4/330 SUN workstation with 32 MB memory.

The iterative application of the approximate inverse mapping has the following general properties. The reduction in misfit is rapid at the early iterations and even a single iteration of the AIM inversion produces a model that is greatly superior to that obtained from the application of an approximate inverse mapping applied to the data. Prolonged execution of the inversion, however, generally increases the structural complexity of the model and may result in an increasing misfit and hence divergence of the algorithm. It is not guaranteed that the minimum misfit will be acceptably small even though the results presented here are encouraging in this regard. Therefore, the method is best used as a means to generate a conductivity model which reduces the data misfit to a low level with minimum computational effort. The resulting model can be used to draw geologic conclusions or it may be used as an initial model for a more rigorous inversion.

ACKNOWLEDGMENTS

We are grateful to FMC Gold Company and Premier Geophysics for making the field data set available to us. We

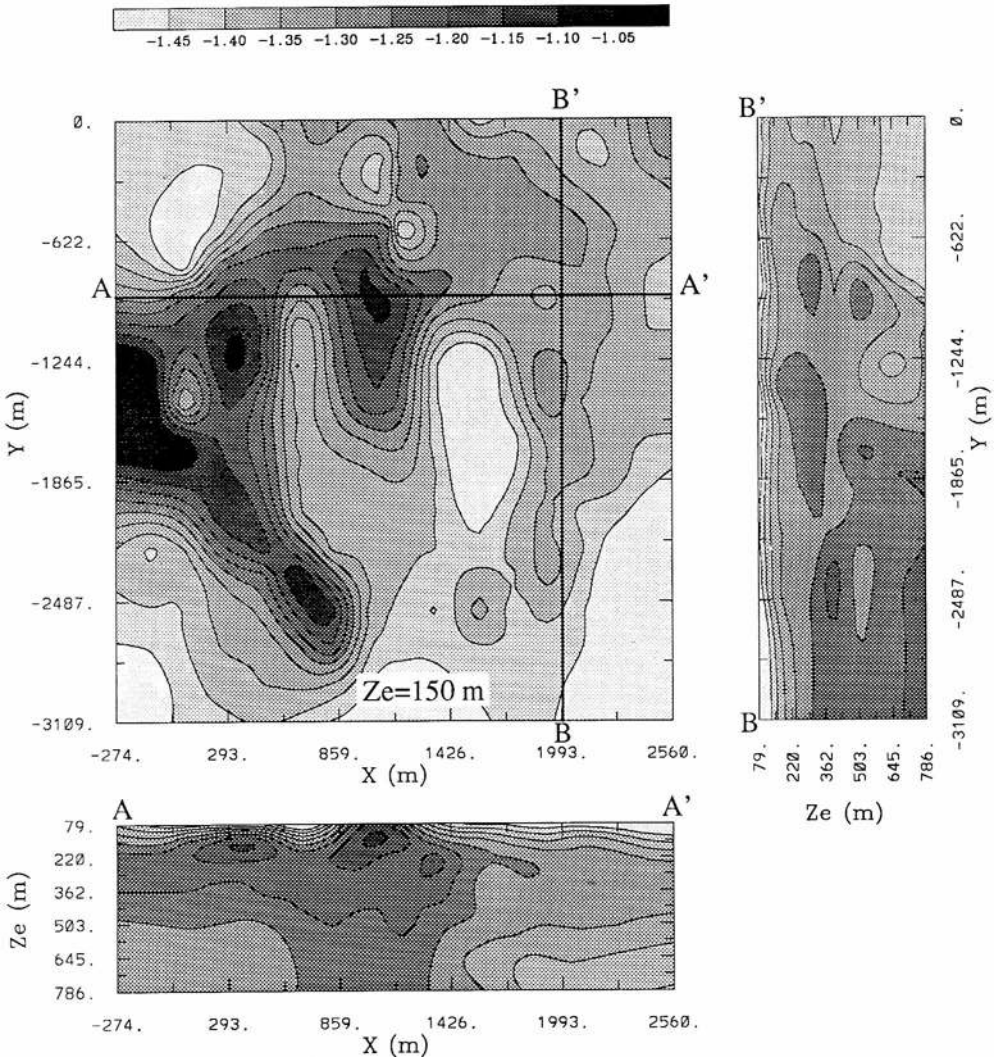

Figure 11. One horizontal slice and two cross-sections of the conductivity model recovered from the field data. The horizontal slice is at a depth of 150 m. The cross-sections are at the same locations as those in Fig. 9.

thank Rob Ellis for many useful discussions pertaining to this research. This work was supported by an NSERC/Industry CRD grant 5-80141.

REFERENCES

Bertero, M., De Mol, C. & Pike, E. R., 1988. Linear inverse problems with discrete data: II. Stability and regularisation, *Inv. Prob.*, **4,** 573–594.

Craven, P. & Wahba, G., 1979. Smoothing noisy data with spline function: estimating the correct degree of smoothing by the method of generalized cross-validation, *Numer. Math.*, **31,** 377–403.

Dey, A. & Morrison, H. F., 1979. Resistivity modelling for arbitrarily shaped three-dimensional structures, *Geophysics,* **44,** 753–780.

Li, Y. & Oldenburg, D. W., 1992. Approximate inverse mappings in DC resistivity problems, *Geophys. J. Int.*, **109,** 343–362.

Li, Y., 1992. Inversion of three-dimensional direct current resistivity data, *PhD thesis,* University of British Columbia, Vancouver.

Oldenburg, D. W. & Ellis, R. G., 1991. Inversion of geophysical data using an approximate inverse mapping, *Geophys. J. Int.*, **105,** 325–353.